Platinum electrochemistry through a magnifying glass

Jacobse, L.

3 Atomic-scale identification of the electrochemical roughening of platinum

Electrode degradation under oxidizing conditions is a major drawback for large scale applications of platinum electrocatalysts. Subjecting Pt(111) to oxidation-reduction cycles is known to lead to the growth of nanoislands. We study this phenomenon using a combination of simultaneous in situ electrochemical scanning tunneling microscopy and cyclic voltammetry. Here, we present a detailed analysis of the formed islands deriving the (evolution of the) kinetic-average island shape. From the island shapes, we determine the densities of atomic-scale defect sites, like steps and facets, which show an excellent correlation to the different voltammetric hydrogen adsorption peaks. Thus, we can directly attribute the hydrogen peaks to the presence of individual surface sites. This delivers new insights into the growth and evolution of the nanoislands as well as into the degradation of real electrocatalysts.

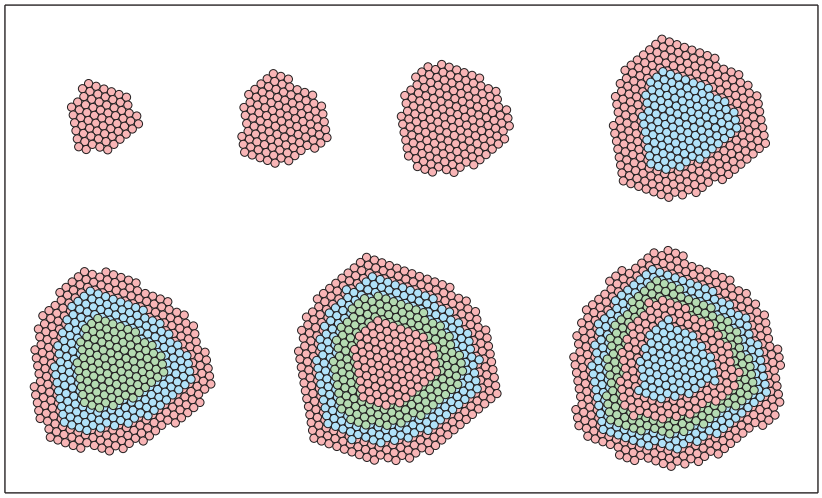

This chapter is based on Jacobse, L., Rost, M.J. & Koper, M.T.M. submitted.

Subjecting a platinum electrode to oxidation-reduction cycles (ORCs) is one of the most commonly performed experiments in surface electrochemistry. This pre-treatment cleans the platinum surface and results in a reproducible (albeit typically unknown) surface structure.[1–3] It is well-known that the Pt surface undergoes a significant structural transformation during this process, as is most dramatically illustrated when starting with a well-defined Pt(111) single crystal electrode.[4] Understanding the roughening of a Pt(111) electrode by ORCs at the atomic scale has therefore been a long-standing goal in fundamental electrochemistry.

Voltammetric experiments provide a fingerprint of the average surface structure, as the adsorption and desorption of hydrogen is very sensitive to the atomic scale surface sites available for this reaction. However, without direct, *in situ* spatial information, data from cyclic voltammetry (CV) alone have been insufficient to describe the (evolution of) the surface structure at the atomic scale.[4–6] On the other hand, spatially resolved data, from *ex situ* low energy electron diffraction (LEED)[7,8], *in situ* x-ray reflectivity[9–16], and *in situ* electrochemical scanning tunneling microscopy (EC-STM)[17–23] experiments, have also not been able to explain the complex evolution of the electrochemical fingerprint signal. By combining *in situ* EC-STM with CVs in a single experiment, we have recently demonstrated that the growth of nano-scale islands, and therefore the electrode roughness, is directly correlated to the integrated hydrogen desorption in the voltammetric signal. This integrated correlation, however, is 'blind' to the different contributions from individual local surface geometries/sites.

In this chapter, we extract the kinetic, atomic-scale nanoisland shape (as a function of the number of applied ORCs) from the EC-STM images and use these shapes to determine the densities of specific undercoordinated ('defect') sites, like steps, facets, and kinks. Furthermore, we disentangle the hydrogen desorption region of the CVs, measured in the same experiment, to quantify the different 'defect'-related contributions. Correlating these two sets of data allows for a direct determination of the reactivity of the different sites that are present at the roughened Pt surface. Therefore, we can pinpoint the individual peaks in the electrochemical hydrogen adsorption signal to specific surface sites. Additionally, this information forms crucial input for understanding the stability of platinum electrodes under potential cycling conditions, and it also provides insight into the interpretation of the voltammetric features of a wide variety of Pt samples, from single crystal surfaces to nanoparticles.

3.1 Electrochemical measurements

The desorption of underpotential deposited hydrogen (H_{UPD}, $0 < U_s < 0.4$ V) contains detailed information on the present average atomic surface structure. Initially, this region only shows a very broad, flat feature related to the hydrogen desorption from the atomically smooth (111) terraces, as indicated by the black line in Fig. 3.1. From this starting situation, the sample potential is cycled between 0.06 and 1.35 V (at 50 mV·s^{-1}), leading to the growth of nanoislands as was shown in Chapter 2. Simultaneously, the electrochemical fingerprint changes drastically, as shown in Fig. 3.1 from blue to red. The appearance of four distinct new peaks, labeled A_{1-4}, indicates the formation of new surface geometries.

To enable a correlation of the CV features to the site densities in the average atomic-scale island shape determined from the STM images, it is necessary to disentangle the charge corresponding to these four H_{UPD} peaks. Several approaches are presented, for single crystalline and nanoparticle samples, in the literature.[24–27] However, especially for very complex surfaces, deconvoluting the

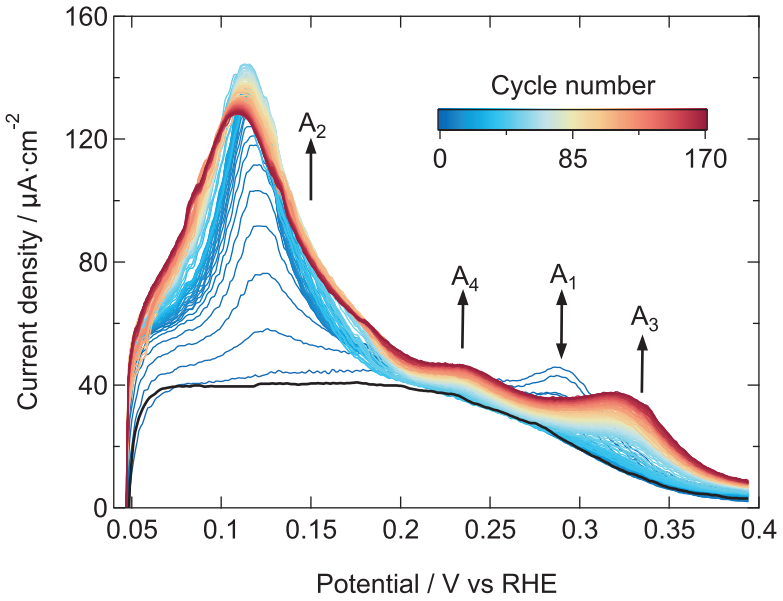

Fig. 3.1 | Evolution of the electrochemical fingerprint upon surface roughening: H_{UPD} region of the 170 subsequent (from blue to red) oxidation-reduction cycles between 0.06 and 1.35 V. The CV of the initial, well-prepared Pt(111) surface is shown in black. Four 'defect'-related peaks, labeled A_{1-4}, are observed during the overall process. The potential scan rate is 50 mV·s^{-1} and the electrolyte is 0.1 M $HClO_4$.

H_{UPD} region shows some discrepancy with results from other electrochemical experiments.[24,26] One of the underlying reasons for this is that the broad (111) terrace feature (black line in Fig. 3.1) changes its shape for more narrow terraces and, overlaps with all four 'defect' peaks.[28] Thus, the terrace feature is typically considered to be a background signal.[6] In our fitting procedure, we therefore also follow this approach by keeping the terrace contribution constant for all cycles. As the number of terrace sites is expected to decrease during the surface roughening, we most likely underestimate the charge related to H_{UPD} at 'defects'. One could imagine to further refine the fitting procedure by using additional data from e.g. regular single crystals or the EC-STM site densities to constrain the fit functions. Such corrections could prove valuable in a more accurate determination of the correlation prefactors (vide infra), but are beyond the scope of this study, as here we aim here for pinpointing certain sites to certain peaks only. Following McCrum and Janik, the broad terrace feature is fitted with an inverse hyperbolic cosine function and the A_{1-4} peaks are fitted with gaussians.[26] To capture the changing shape of the A_2 peak, it is necessary to use a summation of two gaussians. More information on the fit and its quality is provided in Appendix C.

Figure 3.2A shows the integrated charges of the A_{1-4} peaks in the CVs as a function of the number of applied ORCs. The overall process can be separated in different regimes: both the A_1 and A_2 peaks increase during the first few ORCs, then A_1 disappears while A_2 keeps increasing continuously. After prolonged cycling, the A_3 and A_4 peaks appear after 36 and 60 ORCs, respectively. The A_1 and A_2 peaks (and their evolution) have been studied in detail and were ascribed to the presence of {100} and {111} steps at the surface, respectively.[4–6] It is expected that steps form during the roughening of an atomically flat surface. However, it is striking that the charge underneath the A_2 peak is increases continuously, whereas the A_1 peak shows a maximum after two cycles, and subsequently decays to copmletely disappear after 10 ORCs. Based on its peak potential, one expects the A_3 peak to be related to the formation of {100} terraces.[29,30] The A_4 peak is also known as *'the third hydrogen peak'*.[31,32] Although the exact origin of this peak is heavily debated, it appears to be related to the presence of (1x2){110} sites at the surface. Especially for the latter two peaks, it is not clear *a priori* how and if the expected atomic geometries are formed on the roughened surface. Finally, it is important to stress that the A_2 peak changes shape and peak potential upon prolonged potential cycling. This could indicate that this peak actually consists of more than one contribution.

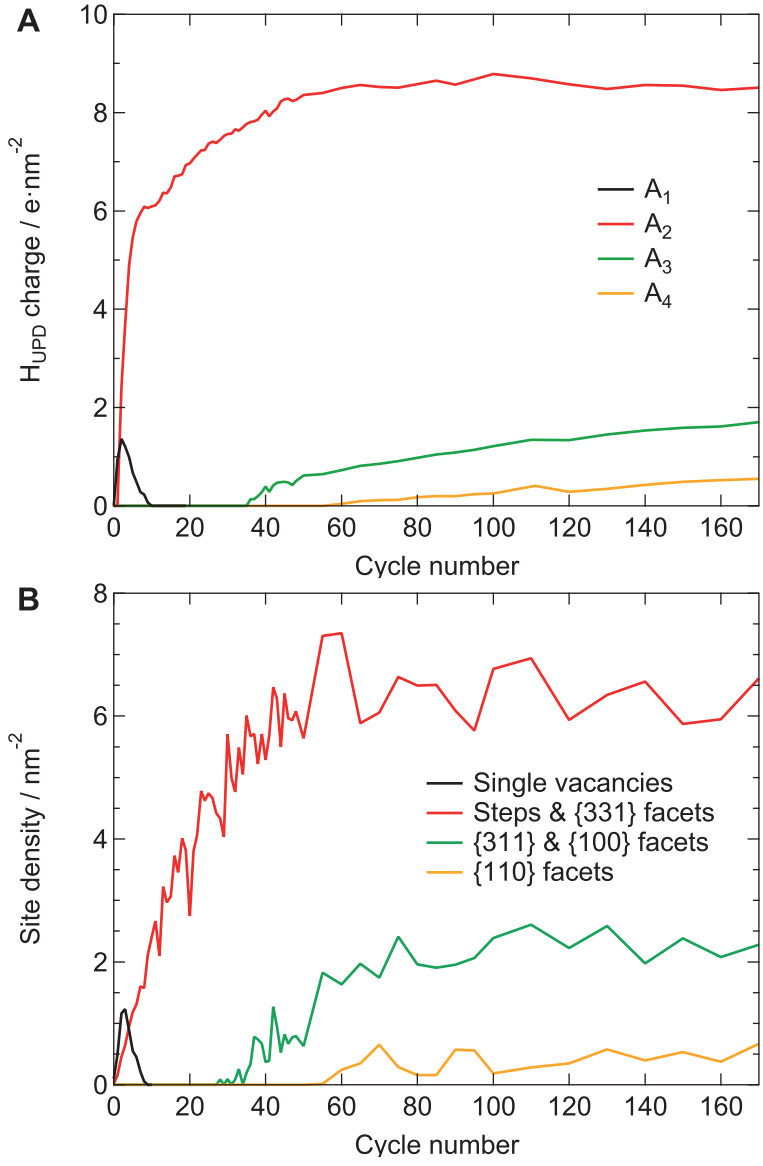

Fig. 3.2 | Evolution of peak charges and corresponding adsorption site densities: (A) The integrated charges of the A_{1-4} peaks in the H_{UPD} region shown in Fig. 3.1. **(B)** The densities of single vacancies, step sites + {331} facets, {311} + {100} facets, and {110} facets as counted from the average atomic-scale island shapes in Fig. 3.3B. Note that {221} and {211} facets (blue in Fig. 3.4) exhibit the same reactivity as 'separated defects' (see main text). Further motivations behind grouping (correlating) the various sites are provided in the main text.

3.2 EC-STM site densities

In the following, we discuss the origin of the evolution of the electrochemical fingerprint signal by the determination of surface site densities extracted from the average island shapes from the EC-STM images. The result of this analysis is already shown in Fig. 3.2B for comparison.

Figure 3.3A shows parts of the EC-STM images after 0, 4, 8, 15, 28, 50, and 170 ORCs. These images have been selected from the full set of 230x230 nm^2 images (see Fig. 2.2 and Ref. [33]), which have been measured with constant tip and sample potential (0.45 and 0.4 V, respectively). With a pixel density of 2.25 Å·$pixel^{-1}$, our images are not directly atomically resolved. In addition, considering the surface roughness and tip convolution, full atomic resolution would be extremely challenging. Nonetheless, the average atomic-scale island shape representative for a certain number of ORCs can be determined by a careful and detailed data analysis, described in Appendix C. In brief, the images are corrected for drift and height offset; approximate island centers are determined by treshold and watershed functions; and island boundaries are determined by a combination of Laplace filtering and the construction of Voronoi cells. In the next step, height profiles of all individual islands present in one EC-STM image are averaged, using the local maximum as island center. Finally, the average island shape is fitted with an fcc lattice, taking into account the main step directions on the surface.

From repeated experiments (see Appendix C) we argue that the shapes of the islands on our wide terraces are not affected by the step edges present. Thus, any asymmetry deviating from the threefold symmetry of the Pt(111) surface originates from the shape of the STM tip. To minimize this imaging artefact, the fitting procedure imposes a threefold island symmetry. In Chapter 2, we have already shown that the area visualized in our EC-STM images can be used to describe the roughening of the entire Pt(111) surface. Except for the first cycles, when the island density is rather low, the analysed areas typically contain between 400 to 500 individual islands. Because of the large number of averaged islands, the resulting island structure is considered to be representative of the statistical growth shape after a certain number of ORCs.[34] Note that such growth shapes differ from classical Wulff shapes in thermodynamic equilibrium.

The results of the fitting procedure for the EC-STM images in Fig. 3.3A are depicted in Fig. 3.3B. The full series of island structures is provided as a movie in Appendix D. From the atomic island structures it is now possible to determine the

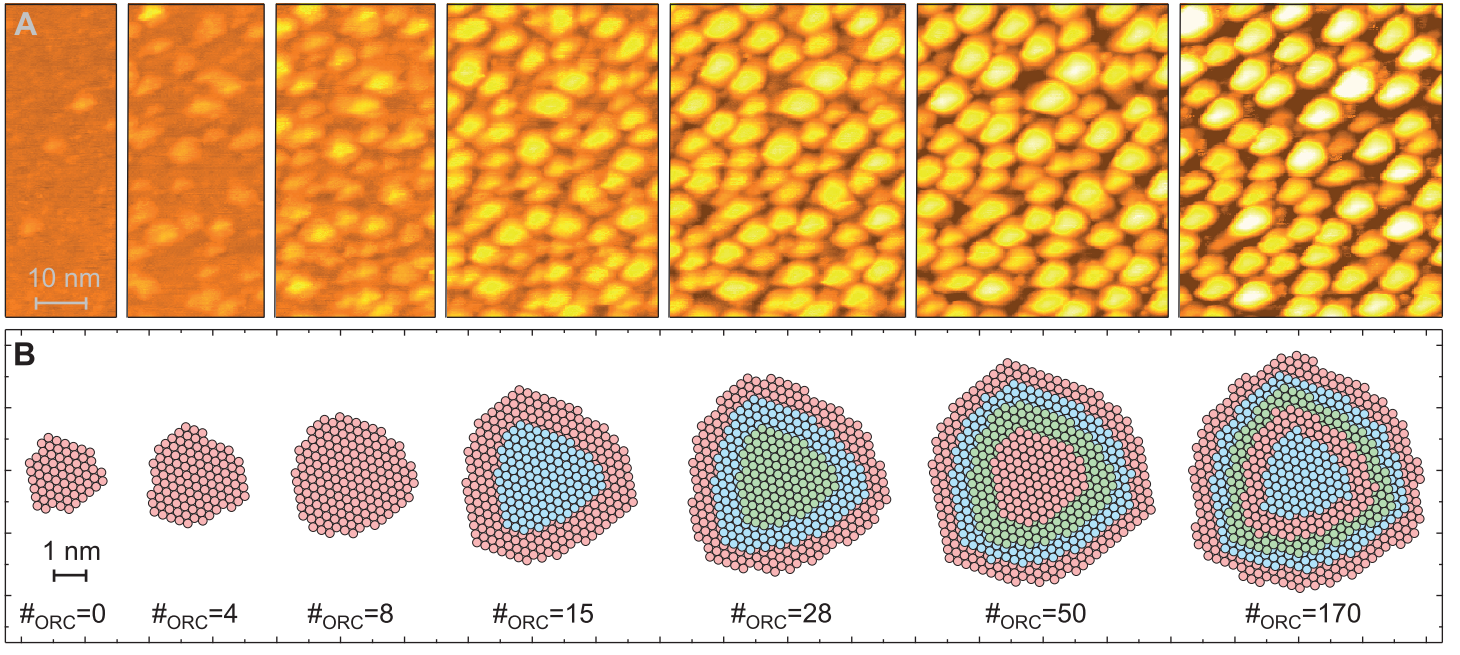

Fig. 3.3 | EC-STM images and average nanoisland structures: **(A)** parts of EC-STM images after 0, 4, 8, 15, 28, 50, and 170 ORCs (from left to right) illustrating the roughening of a single surface area. The original, individual images are 230x230 nm^2, recorded with U_{tip}=0.45 V, U_{sample}=0.4 V, and $I_{tunneling}$ <300 pA. Note that the total contrast is the same for the different images. The full set of EC-STM images is available in Ref. [33]. **(B)** The average atomic-scale growth structure of the islands as determined from the EC-STM images for the same situations as shown in (A). The different colors indicate the different atomic layers in the island. The full image sequence is provided in Appendix D.

densities of the different sites at the surface. Detailed descriptions and counting rules for the various surface geometries can be found in Appendix C, but we provide here the general considerations. Due to the symmetry of the Pt(111) surface, we distinguish three different directions in the surface plane as shown in Fig. 3.4A-C. In the following, we will refer to these directions according to the step site geometry at the corresponding side of the island: {111} steps are found at the {111}-side (Fig. 3.4A) and {100} steps at the {100}-side (Fig. 3.4C). Step edges in the third direction, oriented at midangle between these two densely packed directions, are typically described as '100% kinked'.[35] As these steps have a {112} geometry, we label this as the {112}-side (Fig. 3.4B). Note that for the {111}-side, a rectangular {110} step unit cell is used for counting. This simplifies the site assignment of the total surface, as the {110} unit cell is orthogonal to the step direction.

Additionally, the spacing between 'defects' (steps) in the different layers is known to have a significant effect on their electrochemical reactivity.[28] Step edges that are separated by less than two terrace atoms (as on the (221) and (211) surfaces) bind hydrogen stronger, indicated by a more positive peak potential, than wider spaced step edges. To capture this effect, we consider: (1) step edges separated by more than two terrace atoms ('separated defects', e.g. {110} and {100} steps); (2) step edges separated by two terrace atoms ('wide facets', e.g. {221} and {211} facets); (3) step edges separated by one terrace atom ('narrow facets', e.g. {331} and {311} facets); and (4) adjacent step edges ('low index facets', e.g. {110} and {100} facets). Unit cells of the steps and facets for both the {111}- and {100}-side are shown in Fig. 3.4A and C, respectively. The terrace width is also taken into account at the {112}-side (see Fig. 3.4B) and when counting corner and kink sites as explained in Appendix C. Finally, we also take into account that terrace sites that are adjacent to a 'defect'-site could exhibit a different reactivity. Corner and kink sites occur not only at very low density, but also show a large variation in density between between subsequent ORCs. Sites related to the {112}-side occur at slightly higher densities than kinks, but again with large variations. These variations are most likely fitting artifacts. In the rest of our analysis, we will, therefore, group all different 'defect' sites according to the two most prominent island sides (i.e. the {111}- and {100}-side) and the four different terrace widths (facets) shown in Fig. 3.4A-C. The densities of these eight different groups of sites as a function of cycle number are shown in Fig. 3.4D. It is important to note that kinks at the {111}-side are, due to their geometry, classified as belonging to the {100}-side and *vice versa*.[36]

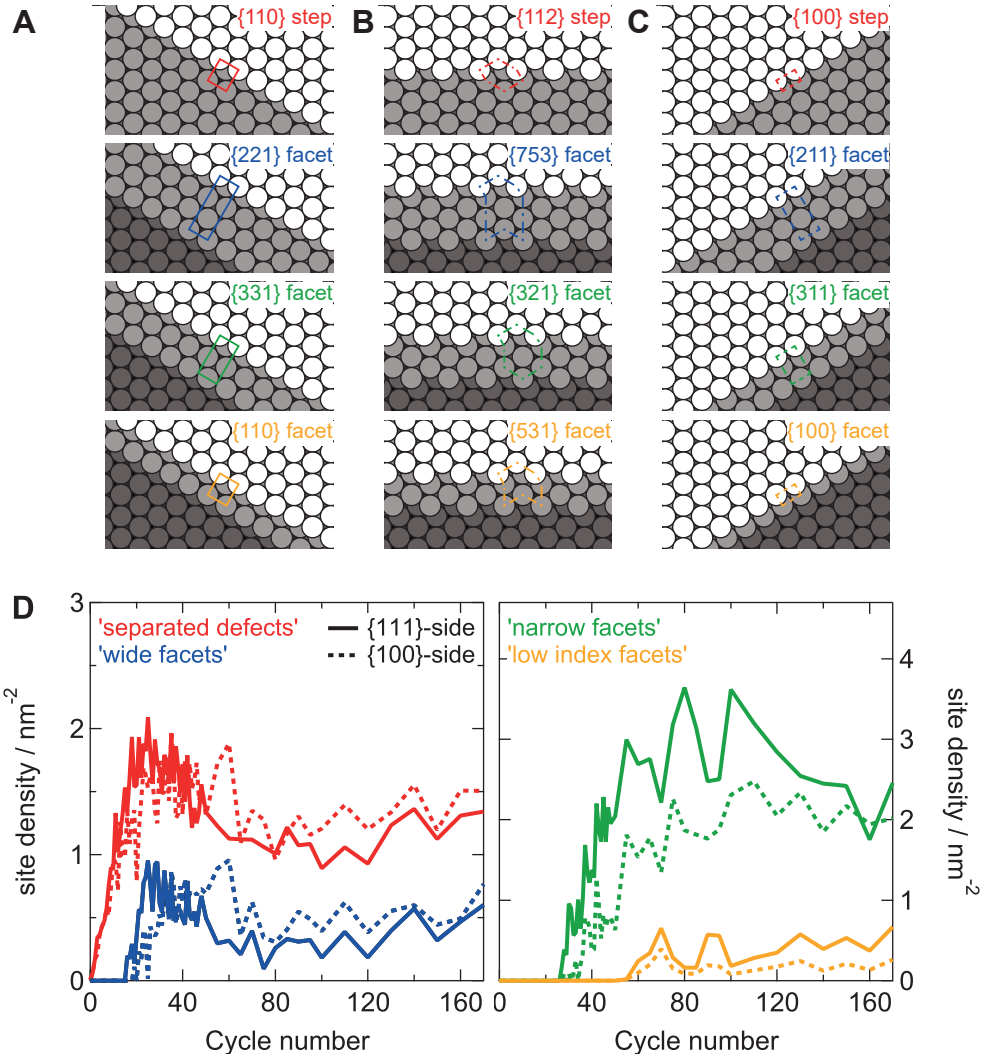

Fig. 3.4 | Unit cells and time evolution of 'defect' site densities derived from average nanoisland structures: **(A-C)** Representative unit cells for the {111}, {112}-, and {100}-side step/facet geometries, respectively. The structures range from 'separated steps' (top) to 'low index facets' (bottom). All counting rules and unit cells for other possible structures, as well as all individual site densities are provided in Appendix C. **(D)** Site densities for the 'separated defects' & 'wide facets' (left), and 'narrow facets' & 'low index facets' (right) for both the {111}- and {100}-side (solid and dashed lines respectively).

Figure 3.4D shows that, initially, only 'separated defects' form, whereas the different kinds of facets only appear after prolonged potential cycling (after 16, 27, and 55 ORCs for 'wide', 'narrow', and 'low index' facets, respectively). This is in line with the observations in Chapter 2, where we described that the nanoislands first nucleate and (mainly) grow laterally, before growing in height. Height growth, while keeping the island base fixed, leads to the formation of facets. Although the islands are rather symmetric, the formation of facets is initially seen at slightly higher intensity at the {111}-side. This is because the unit cell of a {110} step is longer than that of a {100} step. The number of terrace sites on the island (see Appendix C) first increases, but starts decreasing when facets are formed. Including also the (original) terrace sites that are not part of the island, a continuous decrease is observed.

3.3 Correlating site densities to reactivity

Equipped with both the evolution of the disentangled electrochemical fingerprint and the 'defect' site densities, we now correlate these two sets of data to each other. We start the discussion with the simplest case, i.e. the situation between 10 and 30 ORCs. In this regime of the roughening process, the A_2 peak is the only 'defect' feature in the CV. The absence of the A_1 peak around 0.27 V indicates that there are no {100} steps at the surface. If the {111}-side is, under all conditions, significantly more stable (lower free energy) than the {100}-side, we should observe triangular nanoislands composed of only {111}-sides. However, the images in Fig. 3.3B, e.g. after 15 ORCs, clearly show extended 100-type step lengths existing in the island shape. The site densities in Fig. 3.4D also clearly indicate substantial densities of {100} step sites. The only way to explain the significant step length at the {100}-side of the island without the actual formation of {100} step sites is by assuming that these step edges are in reality 'roughened'* and thereby composed of small segments of {110} steps as illustrated in Fig. 3.5. This hypothesis is supported by literature data on the roughening of Pt(11 10 10), a surface which naturally contains regular {100} steps. These data show that {100} step edges are highly unstable during the ORCs: their voltammetric feature diminishes quickly upon potential cycling (almost completely during the first ORC) and is replaced by a {110} feature.[6] Similar observations were made by Rodes and Clavilier, who

* Note that, strictly speaking, step roughening occurs already at each temperature unequal to 0 K, as there is always enough entropy to place a kink into a step: one only has to increase the step lengths.[36]

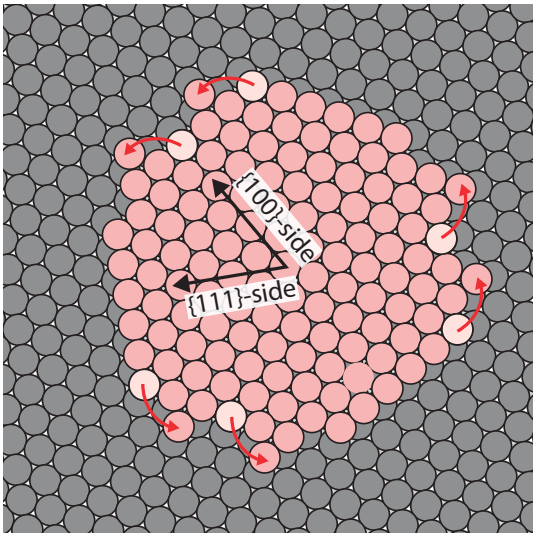

Fig. 3.5 | Step 'roughening' example: Example of a (mass conserved) step 'roughening' to minimize the number of {100} step sites. Such step structures are necessary to explain the island symmetry in combination with the presence of only one 'defect' peak in the CVs between 10 and 30 ORCs, see Fig. 3.2.

studied the electrochemical behavior of various single crystal surfaces with {100} step edges as a function of annealing/cooling conditions and potential cycling.[37]

The 'roughened' hexagonal islands (Fig. 3.5) will only be preferred over triangular islands if the step sites at the {100}-side are stabilized somewhere during potential cycling. This expectation is supported by DFT calculations, which indicate that Pt(100) is more stable than Pt(110) at high potentials (>0.9V for the surface oxide and >1.05 V for adsorbed O/OH).[38] Unfortunately, the step edge 'roughening' is not captured in our fitting results. The reason for this is both the averaging process for the determination of the average island shape and the limited resolution of our EC-STM images. The study by Rodes and Clavilier has shown that when 'separated' step edges are roughened, the increase in charge of the A_2 peak is twice the decrease in charge of the A_1 peak.[37] This is ascribed to the formation of two kink sites from one step site. Thus, in our correlation analysis we argue that each 'separated' {100} step site contributes double to the A_2 peak. The facets at the {100}-side and their 'roughening', which could also contribute to the A_2 peak, are discussed below.

Let us now focus on the A_3 and A_4 peaks, which appear after further potential cycling. Their 'late' appearance indicates that they are related to the formation of specific facets due to the height growth of the nanoislands. This is confirmed when inspecting the average island shape after 28 ORCs in Fig. 3.3B: all standard step and kink sites are present, but the A_3 and A_4 peaks do not yet contribute to the CV. The charge of the A_3 peak is clearly correlated to the density of {311} facet sites (correlation coefficient r=0.92, see Appendix C). This is in line with the A_3 peak potential (~0.32 V), which is slightly higher than that of {100} step sites.[28] Interestingly, this correlation must also mean that the {311} facet is stable enough to withstand the step edge 'roughening', which occurs for the 'separated' {100} step sites. Indeed, roughening experiments of Pt(311) by thermal or electrochemical adsorption of oxygen do not show any formation of {110} step/kink sites. The stabilization of straight step edges for narrow terraces can be ascribed to the repulsive interaction between step edges of equal sign[36] and has been observed before for stepped Pt surfaces.[39] Literature data is not consistent on the stability of the {211} facet. Thermal oxidation experiments indicate that this step edge also withstands step 'roughening'[37], but potential cycling experiments suggest the opposite.[40] As the {211} facets appear 10 cycles before the emergence of the A_3 peak, we conclude that also this facet must roughen and thus contribute to the A_2 peak instead. Most likely, the {100} facets contribute as well to the A_3 peak.[28] Indeed, the summation of the densities of {311} and {100} facets (the green line in Fig. 3.2B) leads to a slightly higher correlation coefficient (0.93, see Appendix C).

As the A_4 peak appears later than the A_3 peak, it is expected that this peak is related to the formation of facets that are even narrower than the {311} facets. Considering the peak potential, these sites are likely formed at the {111}-side of the islands. Nonetheless, the correlation between the {110} facets (yellow line in Fig. 3.2B) and the A_4 charge is rather low (r=0.54). Upon closer inspection (see Appendix C), it becomes clear that this is mainly due to the large variation in the density of {110} facets between subsequent cycles. After applying a moving average filter (averaging over 5 data points) to the {110} facet density, the correlation coefficient is significantly increased (r=0.93, see Appendix C).

The A_2 peak for the roughened surface is much broader than for a regularly stepped single crystal. This complicates the separate identification of {111}-side facets, as these features overlap in our CVs. The better correlation between the A_2 charge and the site densities when the {331} facet sites are included (r=0.88 vs 0.76)confirms this overlap. The correlation analysis also indicates that the 'wide facets' are better described as 'separated defects', i.e. the adjacent terrace

sites do not contribute to the A_2 peak (see Appendix C). This suggests that the small facet-related features as observed for Pt(221) and Pt(211), are actually due to the terrace width distribution of these surfaces.[28] The summation of all sites contributing to the A_2 peak (all 'separated defects' and the {331} facets) is shown as the red curve in Fig. 3.2B.

Most puzzling is the observation that there is no surface site in the adatom islands that, after appearing during the first two cycles, disappears completely after 10 ORCs, as suggested by peak A_1. Importantly, the islands are only one atom high when this peak is present, which excludes that it originates from the formation of some kind of facet site. One could imagine that this peak is related to the presence of 'separated' {100} step sites which did not yet 'roughen', e.g. due to a very small island size. However, if that would be true, this peak would reappear once a new layer nucleates on top of an existing island, i.e. after 9, 16, 30, and 55 ORCs. This is not the case. Thus, we conclude that this peak must be related to some surface site that is not present in the adatom islands at all. Furthermore, it is also unlikely that this peak originates from a surface miscut. This would neither explain why it increases during the first cycles, nor that the charge is 2-3 orders of magnitude larger than what would be expected for such a signal. In conclusion, we need a surface site that is solely present in the very beginning of the roughening process.

As the surface roughening is (almost completely) mass conserved[41–44], we observed in Chapter 2 (see also Appendix B) that vacancies form simultaneously with the adatom islands. These small vacancies are extremely difficult to resolve in STM and will, especially at low coverages, not contribute to the average island structure. If we neglect the small amount of dissolving Pt under our experimental conditions, the number of single vacancies must be the same as the number of adatoms forming the average island shape. This implies the existence of additional 'defect' features in the form of terrace atoms that are immediately adjacent to a vacancy site. Note that the nucleation of single vacancies into vacancy islands of specific sizes will play a role in the expected current densities. The total electrochemical signal resulting from 'defects' adjacent to a vacancy site can thus be described by:

$$\begin{aligned} j_{vac} &\propto A_{island} \cdot (P_{terrace})^{f(n)} \\ j_{vac} &\propto A_{island} \cdot (1-2 \cdot A_{island})^{f(n)}, \end{aligned} \tag{3.1}$$

where j_{vac} is the expected current density due to vacancy-related steps, A_{island}

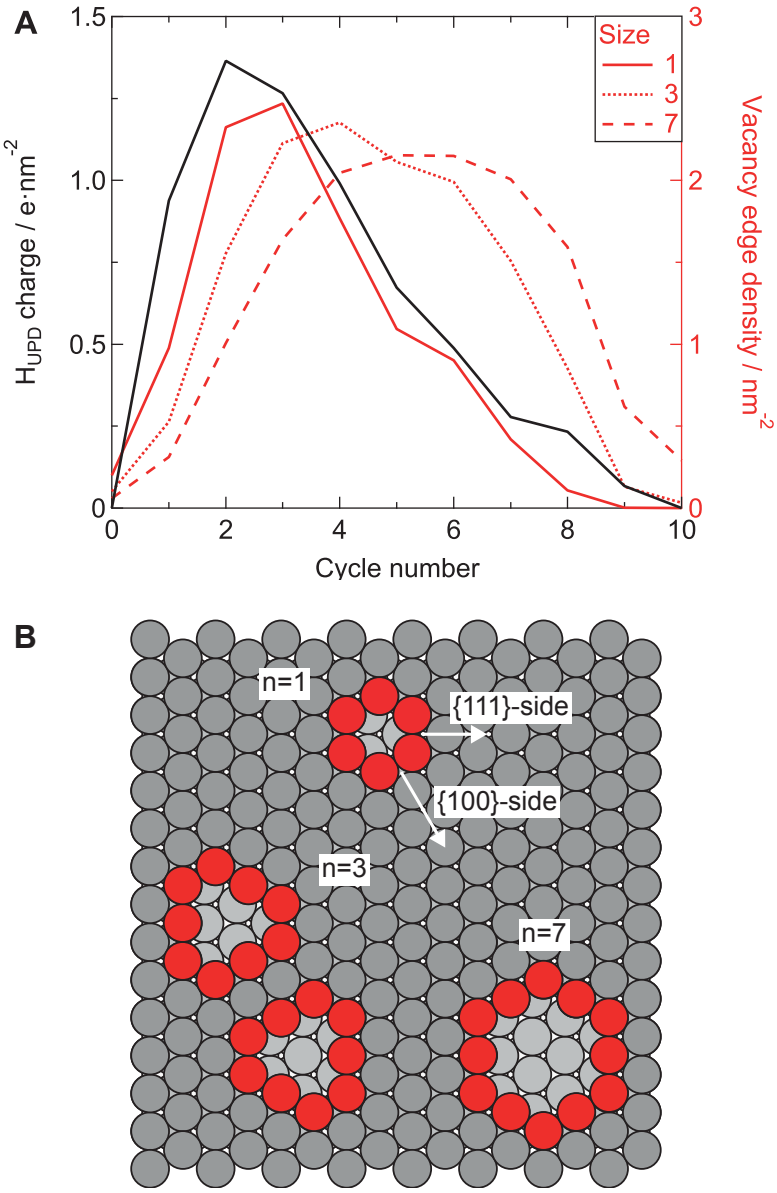

Fig. 3.6 | Vacancy site formation: **(A)** Comparison between the charge of the A_1 peak (black) and the expected vacancy signal (red) according to Eq. 3.1 for single vacancies and vacancy islands of 3 and 7 atoms. **(B)** Affected vacancy edge sites (red) for single vacancies and vacancy islands of 3 and 7 atoms. The arrows at the single vacancy indicate the two nonequivalent directions. Note that two two different island orientations exist for the n=3 vacancy island.

is the adatom island coverage, $P_{terrace}$ is the probability that the adjacent site was originally a terrace site (i.e. not a vacancy or adatom site), and $f(n)$ is the number of adjacent terrace sites per vacancy site that has to be present to form a vacancy island of size n (i.e. $f(1)$=6, $f(3)$=3, $f(7)$=$\frac{12}{7}$). Note that the distribution and existence of single vacancies and vacancy islands in a Pt(111) surface can be significantly more complicated, as this surface is on the verge of forming a reconstruction.[45–47]

Figure 3.6A shows the expected vacancy signal (red) for the formation of single vacancies and for vacancy islands of 3 and 7 atoms (so-called magic clusters[48]) together with the charge underneath the A_1 peak (black). The corresponding structures are shown in Fig. 3.6B. The best correlation to the charge of the A_1 peak (r=0.96) is obtained when we take into account the formation of single, isolated vacancies. This signal is also shown as the black curve in Fig. 3.2B. Considering the simplicity of our approach, the level of correlation is remarkable. When the A_1 peak reaches its maximum, the distance between the vacancies would only be 3-4 atoms. At these (and higher) coverages, one would expect to observe the nucleation of vacancy islands. Thus the total signal would become a weighted average of the different curves shown in Fig. 3.6A, leading to an additional tail after more ORCs. On the other hand, individual vacancy formation is likely to occur within (larger) vacancy islands. In any case, we can conclude that the A_1 peak is related to the formation of vacancy sites, although the full explanation will likely be more complex than our simple model.

The peak potential of the A_1 peak suggests that its signal originates only from {100} sites. As the correlation prefactor is close to two (see the y-axes of Fig. 3.6A and the discussion below), it is tempting to argue that the vacancies lead to the formation of equal amounts of both {100} and {110} step sites. Although a step edge description is probably not directly valid for single vacancies, it is clear that these sites have two nonequivalent sides, as indicated in Fig. 3.6B. Upon nucleation of vacancy islands, 'step roughening' could occur such that the vacancy-related 'defects' now only contribute to the A_2 peak. However, with the limited information we have on the vacancy sites, it seems impossible to disentangle this signal. Nevertheless, Fig. 3.2 indicates that during the first ~20 cycles, the number of sites contributing to the A_2 peak is underestimated (see also Appendix C). The discrepancy is largest during the first three ORCs and then diminishes, which hints at a relationship to the formation of vacancy (island) sites.

The analysis above shows that site densities extracted from EC-STM images are in very good accordance with the evolution of the cyclic voltammetry during the surface roughening. Finally, it is interesting to look at the prefactors of the correlations, which are worked out and shown in detail in Appendix C. In the traditional picture of adsorption/desorption of a single hydrogen atom at each 'defect' site, one would expect all prefactors to be unity.[37,49–51] However, recent studies demonstrate that the 'defect' features in the H_{UPD} region are actually not just adsorption/desorption of hydrogen, but rather a replacement of hydrogen atoms by hydroxyl groups.[52,53] As a result, the expected transferred charge per surface site is somewhat larger than 1 e^-. Experimental results point in this direction, albeit without quantification, for widely spaced {110} step edges[54]. However, it is not directly clear to what extent these values are affected by the applied fitting procedure. Our prefactors for the A_1 and A_2 peaks (1.07 ± 0.07 and 1.46 ± 0.04 e^-/site, respectively) match these expectations. The prefactors for the A_3 and A_4-peaks (0.56 ± 0.02, and 0.77 ± 0.06 e^-/site, respectively), on the other hand, seem to be too small. However, this can be explained by our fitting procedure, in which we keep the terrace contribution constant. Single crystal experiments show that the broad (111) terrace feature changes shape, i.e. loses intensity mainly at high potentials, due to the formation of narrow terraces.[28] This leads to an underestimation of the 'defect'-peaks, in particular the A_3 and A_4 peaks, which appear with narrowing terraces. Finally, one should be aware of the limitations of counting absolute site densities from the EC-STM images. As it is impossible to fully correct for tip convolution effects, there will always be some uncertainty in the determined densities; the size of the islands will be slightly overestimated, whereas the depth of the 'holes' in between the islands is not fully resolved. Another uncertainty comes from the step edge 'roughening', which is also not directly measured. Finally, the available literature data for kinked surfaces is not sufficient to rigorously proof that the corner and fully-kinked step 'defects' contribute equally to the {100} and {110}-related CV features. This was an underlying assumption of grouping the site densities as performed in Fig. 3.4D. Thus, although the current values of our prefactors are in the right range, they should be interpreted with some care.

3.4 Conclusions

In this chapter, we have shown that the complex evolution of the electrochemical fingerprint of a Pt(111) surface upon ORCs can directly be explained from the (evolution of the) densities of various surface sites. Thus, our analysis provides direct evidence for the electrochemical response of individual 'defect' sites. It provides a solid background for the interpretation of the electrochemical response not only of rough (e.g. polycrystalline) platinum surfaces in general, but also for nanoparticles, and even regularly stepped single crystal surfaces. The atomic description of the roughening process also leads to a better understanding of the stability of specific atomic geometries under potential cycling conditions. These insights form valuable input for the further development of platinum electrocatalysts that exhibit both a high activity and a long lifetime.

References

1. Bard, A. J. & Faulkner, L. R. *Electrochemical methods : fundamentals and applications* 833 (Wiley, 2001).
2. Schmickler, W. and Santos, E. *Interfacial electrochemistry* 272 (Springer-Verlag Berlin Heidelberg, 2010).
3. Santos, E. and Schmickler, W. *Catalysis in Electrochemistry: From Fundamental Aspects to Strategies for Fuel Cell Development* 516 (John Wiley & Sons, Inc., 2011).
4. Gómez-Marín, A. M. & Feliu, J. M. Pt(111) surface disorder kinetics in perchloric acid solutions and the influence of specific anion adsorption. *Electrochim. Acta* **82,** 558–569 (2012).
5. Björling, A., Ahlberg, E. & Feliu, J. M. Kinetics of surface modification induced by submonolayer electrochemical oxygen adsorption on Pt(1 1 1). *Electrochem. commun.* **12,** 359–361 (2010).
6. Björling, A. & Feliu, J. M. Electrochemical surface reordering of Pt(111): A quantification of the place-exchange process. *J. Electroanal. Chem.* **662,** 17–24 (2011).
7. Wagner, F. T. & Ross, P. N. LEED spot profile analysis of the structure of electrochemically treated Pt(100) and Pt(111) surfaces. *Surf. Sci.* **160,** 305–330 (1985).
8. Aberdam, D., Durand, R., Faure, R. & El-Omar, F. Structural changes of a Pt(111) electrode induced by electrosorption of oxygen in acidic solutions: a coupled voltammetry, LEED and AES study. *Surf. Sci.* **171,** 303–330 (1986).
9. You, H. & Nagy, Z. Oxidation-reduction-induced roughening of platinum (111) surface. *Phys. B Condens. Matter* **198,** 187–194 (1994).
10. You, H., Zurawski, D. J., Nagy, Z. & Yonco, R. M. In-situ x-ray reflectivity study of incipient oxidation of Pt(111) surface in electrolyte solutions. *J. Chem. Phys.* **100,** 4699 (1994).
11. Nagy, Z. & You, H. Applications of surface X-ray scattering to electrochemistry problems. *Electrochim. Acta* **47,** 3037–3055 (2002).
12. Liu, Y., Barbour, A., Komanicky, V. & You, H. X-ray Crystal Truncation Rod Studies of Surface Oxidation and Reduction on Pt(111). *J. Phys. Chem. C* **120,** 16174–16178 (2016).
13. Goryachev, A. *et al.* Synchrotron based operando surface X-ray scattering study towards structure-activity relationships of model electrocatalysts. *ChemistrySelect* **1,** 1104–1108 (2016).
14. Drnec, J. *et al.* Initial stages of Pt(111) electrooxidation: dynamic and structural studies by surface X-ray diffraction. *Electrochim. Acta* **224,** 220–227 (2017).
15. Ruge, M. *et al.* Structural Reorganisation of Pt(111) Electrodes by Electrochemical Oxidation and Reduction. *J. Am. Chem. Soc.* **139,** 4532–4539 (2017).

16. Ruge, M. *et al.* Electrochemical Oxidation of Smooth and Nanoscale Rough Pt(111): An In Situ Surface X-ray Scattering Study. *J. Electrochem. Soc.* **164,** H608–H614 (2017).
17. Sugawara, S. & Itaya, K. In situ scanning tunnelling microscopy of a platinum {111} surface in aqueous sulphuric acid solution. *J. Chem. Soc. Faraday Trans. 1 Phys. Chem. Condens. Phases* **85,** 1351 (1989).
18. Itaya, K. In situ scanning tunneling microscopy of platinum (111) surface with the observation of monatomic steps. *J. Vac. Sci. Technol. A Vacuum, Surfaces, Film.* **8,** 515 (1990).
19. Sashikata, K., Furuya, N. & Itaya, K. In situ electrochemical scanning tunneling microscopy of single-crystal surfaces of Pt(111), Rh(111), and Pd(111) in aqueous sulfuric acid solution. *J. Vac. Sci. Technol. B Microelectron. Nanom. Struct.* **9,** 457 (1991).
20. Breuer, N., Funtikov, A., Stimming, U. & Vogel, R. In situ electrochemical STM imaging of roughened gold and platinum electrode surfaces. *Surf. Sci.* **335,** 145–154 (1995).
21. Furuya, N. & Shibata, M. Structural changes at various Pt single crystal surfaces with potential cycles in acidic and alkaline solutions. *J. Electroanal. Chem.* **467,** 85–91 (1999).
22. Löffler, T., Bussar, R., Xiao, X., Ernst, S. & Baltruschat, H. The adsorption of ethene on vicinally stepped electrode surfaces and the effect of temperature. *J. Electroanal. Chem.* **629,** 1–14 (2009).
23. Wakisaka, M., Asizawa, S., Uchida, H. & Watanabe, M. In situ STM observation of morphological changes of the Pt(111) electrode surface during potential cycling in 10 mM HF solution. *Phys. Chem. Chem. Phys.* **12,** 4184–4190 (2010).
24. Solla-Gullón, J., Rodríguez, P., Herrero, E., Aldaz, A. & Feliu, J. M. Surface characterization of platinum electrodes. *Phys. Chem. Chem. Phys.* **10,** 1359–1373 (2008).
25. Vidal-Iglesias, F. J., Arán-Ais, R. M., Solla-Gullón, J., Herrero, E. & Feliu, J. M. Electrochemical characterization of shape-controlled Pt nanoparticles in different supporting electrolytes. *ACS Catalysis* **2,** 901–910 (2012).
26. McCrum, I. T. & Janik, M. J. Deconvoluting Cyclic Voltammograms To Accurately Calculate Pt Electrochemically Active Surface Area. *J. Phys. Chem. C* **121,** 6237–6245 (2017).
27. Arán-Ais, R. M., Solla-Gullón, J., Herrero, E. & Feliu, J. M. On the quality and stability of preferentially oriented (100) Pt nanoparticles: An electrochemical insight. *J. Electroanal. Chem.* **808,** 433–438 (2018).
28. García-Aráez, N., Climent, V. & Feliu, J. M. Potential-dependent water orientation on Pt(1 1 1) stepped surfaces from laser-pulsed experiments. *Electrochim. Acta* **54,** 966–977 (2009).
29. Furuya, N. & Koide, S. Hydrogen adsorption on platinum single-crystal surfaces. *Surf. Sci.* **220,** 18–28 (1989).
30. Domke, K., Herrero, E., Rodes, A. & Feliu, J. M. Determination of the potentials of zero total charge of Pt(100) stepped surfaces in the [011] zone. Effect of the step density and anion adsorption. *J. Electroanal. Chem.* **552,** 115–128 (2003).
31. Gómez, R. & Clavilier, J. Electrochemical behaviour of platinum surfaces containing (110) sites and the problem of the third oxidation peak. *J Electroanal Chem* **354,** 189–208 (1993).
32. Diaz-Morales, O., Hersbach, T. J. P., Badan, C., Garcia, A. C. & Koper, M. T. M. Hydrogen adsorption on nano-structured platinum electrodes. *Faraday Discuss.* (2018).
33. Jacobse, L., Huang, Y. F., Koper, M. T. M. & Rost, M. J. Correlation of surface site formation to nanoisland growth in the electrochemical roughening of Pt(111). *Nature Materials* **17,** 277–282 (2018).
34. Sekerka, R. F. Equilibrium and growth shapes of crystals: How do they differ and why should we care? *Cryst. Res. Technol.* **40,** 291–306 (2005).
35. Schulze Icking-Konert, G., Giesen, M. & Ibach, H. Novel method for the experimental determination of step energies. *Phys. Rev. Lett.* **83,** 3880–3883 (1999).
36. Ibach, H. *Physics of Surfaces and Interfaces* 646 (Springer, 2006).
37. Rodes, A. & Clavilier, J. Electrochemical study of step reconstruction on platinum surfaces belonging to the [011] zone between Pt(311) and Pt(111). *J. Electroanal. Chem.* **344,** 269–288 (1993).
38. McCrum, I. T., Hickner, M. A. & Janik, M. J. First-Principles Calculation of Pt Surface Energies in an Electrochemical Environment: Thermodynamic Driving Forces for Surface Faceting and Nanoparticle Reconstruction. *Langmuir* **33,** 7043–7052 (2017).

39. Walter, A. L. *et al.* X-ray photoemission analysis of clean and carbon monoxide-chemisorbed Pt(111) stepped surfaces using a curved crystal. *Nat. Commun.* **6,** 8903 (2015).
40. Clavilier, J., Armand, D., Sun, S. & Petit, M. Electrochemical adsorption behaviour of platinum stepped surfaces in sulphuric acid solutions. *J. Electroanal. Chem.* **205,** 267–277 (1986).
41. Topalov, A. A. *et al.* Dissolution of platinum: Limits for the deployment of electrochemical energy conversion? *Angew. Chem. Int. Ed.* **51,** 12613–12615 (2012).
42. Lopes, P. P. *et al.* Relationships between atomic level surface structure and stability/activity of platinum surface atoms in aqueous environments. *ACS Catal.* **6,** 2536–2544 (2016).
43. Sugawara, Y., Sasaki, M., Muto, I. & Hara, N. Dissolution of Platinum Single Crystal Surfaces under Potential Cycling in Sulfuric Acid Solution. *ECS Trans.* **64,** 81–87 (2014).
44. Rost, M. J., Jacobse, L. & Koper, M. T. M. The Dualism between Adatom- and Vacancy-based Single Crystal Growth Models (to be submitted).
45. Bott, M., Hohage, M., Michely, T. & Comsa, G. Pt(111) reconstruction induced by enhanced Pt gas-phase chemical potential. *Phys. Rev. Lett.* **70,** 1489–1492 (1993).
46. Hohage, M., Michely, T. & Comsa, G. Pt(111) network reconstruction: structure, growth and decay. *Surf. Sci.* **337,** 249–267 (1995).
47. Michely, T., Hohage, M., Esch, S. & Comsa, G. The effect of surface reconstruction on the growth mode in homoepitaxy. *Surf. Sci.* **349,** L89–L94 (1996).
48. Wang, S. C. & Ehrlich, G. Structure, stability, and surface diffusion of clusters: Irx on Ir(111). *Surf. Sci.* **239,** 301–332 (1990).
49. Clavilier, J., El Achi, K. & Rodes, A. In situ characterization of the Pt(S)-[n(111) x (111)] electrode surfaces using electrosorbed hydrogen for probing terrace an step sites. *J. Electroanal. Chem.* **272,** 253–261 (1989).
50. Rodes, A., El Achi, K., Zamakhchari, M. A. & Clavilier, J. Hydrogen probing of step and terrace sites on Pt(S)-[n(111) x (100)] electrodes. *J. Electroanal. Chem.* **284,** 245–253 (1990).
51. Clavilier, J. & Rodes, A. Electrochemical Detection and Characterization at Pt(N,N,N-2) Oriented Electrodes of Multiatomic Step Formation Induced by Quenching at High-Temperatures. *J. Electroanal. Chem.* **348,** 247–264 (1993).
52. McCrum, I. T. & Janik, M. J. pH and Alkali Cation Effects on the Pt Cyclic Voltammogram Explained Using Density Functional Theory. *J. Phys. Chem. C* **120,** 457–471 (2016).
53. Chen, X., McCrum, I. T., Schwarz, K. A., Janik, M. J. & Koper, M. T. Co-adsorption of Cations as the Cause of the Apparent pH Dependence of Hydrogen Adsorption on a Stepped Platinum Single-Crystal Electrode. *Angew. Chem. Int. Ed.* **56,** 15025–15029 (2017).
54. Van Der Niet, M. J., Garcia-Araez, N., Hernández, J., Feliu, J. M. & Koper, M. T. Water dissociation on well-defined platinum surfaces: The electrochemical perspective. *Catal. Today* **202,** 105–113 (2013).